# Interfacial Charge Induced Magnetoelectric Coupling at BiFeO₃/BaTiO₃ Bilayer Interface

Rekha Gupta,[†] Sujeet Chaudhary,[‡] and R. K. Kotnala*,[†]

[†]CSIR—National Physical Laboratory, New Delhi 110012, India
[‡]Department of Physics, Indian Institute of Technology Delhi, New Delhi 110016, India

S *Supporting Information*

ABSTRACT: Bilayer thin films of $BiFeO_3$–$BaTiO_3$ at different thicknesses of $BiFeO_3$ were prepared by RF-magnetron sputtering technique. A pure phase polycrystalline growth of thin films was confirmed from XRD results. Significantly improved ferroelectric polarization ($2P_r$ ~ 30 $\mu C/cm^2$) and magnetic moment (M_s ~ 33 emu/cc) were observed at room temperature. Effect of ferroelectric polarization on current conduction across the interface has been explored. Accumulation and depletion of charges at the bilayer interface were analyzed by current−voltage measurements which were further confirmed from hysteretic dynamic resistance and capacitance voltage profiles. Magnetoelectric coupling due to induced charges at grain boundaries of bilayer interface was further investigated by room temperature magnetocapacitance analysis. A room temperature magnetocapacitance was found to originate from induced charge at the bilayer interface which can be manipulated by varying the thickness of BFO to obtain higher ME coupling coefficient. Dynamic magnetoelectric coupling was investigated, and maximum longitudinal magnetoelectric coupling was observed to be 61 mV/cm·Oe at 50 nm thickness of $BiFeO_3$. The observed magnetoelectric properties are potentially useful for novel room temperature magnetoelectric and spintronic device applications.

KEYWORDS: *ferroelectric, ferromagnetic, multiferroic, magnetocapacitance, magnetoelectric coupling*
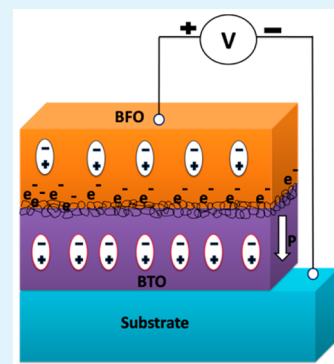
INTRODUCTION

Multiferroic materials are of significant interest in scientific as well as technological requirements due to the possibility of controlling magnetism through electric field.[1,2] The interplay between magnetic and ferroelectric order parameters offers various applications in novel spintronics and magnetoelectric devices with fast speed and low power consumption.[3,4] The artificial multiferroic heterostructure in the form of multi-layer,[5−8] superlattice,[9] and vertically aligned nanopillars[10] has been extensively studied due to their ability to provide new physical insights responsible for induced magnetoelectric (ME) coupling.[11−14] Multiferroic bilayer thin films have been subjected to a wide range of focus due to their interesting magnetoelectric properties. Significantly improved electric as well as magnetic properties can be tailored by appropriate combination of constituent layers. The interfacial effects play a crucial role in deciding ferroelectric, magnetic, as well as magnetoelectric properties of bilayer thin films.[8,15−17] Bismuth ferrite ($BiFeO_3$) is a novel multiferroic material with the simultaneous existence of room temperature antiferromagnet-ism (T_N = 643 K) and ferroelectricity (T_C = 1103 K).[18] The multiferroic properties of $BiFeO_3$ (BFO) have been widely investigated in bulk as well as in thin films. A serious obstacle in the technological application of BFO is its weak magnetic behavior and high leakage current. Although thin films of BFO exhibit much improved ferroelectric polarization and magnetic behavior, still new routes are to be explored to improve its magnetoelectric properties. Bilayer thin films of BFO with

other perovskite ferroelectric materials have been found to be an effective way to reduce its leakage current and improve ferroelectric polarization.[15−24] $BaTiO_3$ (BTO) is one of the lead-free ferroelectric materials which have been very well studied in solid solution form of $BiFeO_3$ −$BaTiO_3$, and few studies are also available on thin films based upon these solid solutions.[20,25−29] Magnetoelectric properties of bilayer thin films of BFO−BTO are rarely reported. In this work, we have prepared bilayer thin films of BFO/BTO at Pt/Ti/SiO₂/Si(100) substrate with different thicknesses of BFO with an objective to understand the influence on the multiferroic properties and magnetoelectric coupling interaction mediated by the nature of interface between the two layers.

EXPERIMENTAL SECTION

Bilayer thin films of BFO/BTO were prepared on Pt/TiO₂/SiO₂/Si(100) substrate by RF-magnetron sputtering technique. Targets of $BiFeO_3$ and $BaTiO_3$ were synthesized by conventional solid state reaction method. BTO layer was first deposited on Pt/Ti/SiO₂/Si(100) substrate maintained at a temperature of 650 °C followed by subsequent deposition of BFO layer on BTO/Pt/Ti/SiO₂/Si(100) at the same substrate temperature. The deposition was carried out at 50 mTorr in a mixture of Ar and O₂ in the ratio of (4:1) with a base pressure of 3×10^{-6} Torr. The thickness of BTO layer was kept fixed at 100 nm while BFO layer was deposited for different thicknesses of

50 nm (BFBT-5), 100 nm (BFBT-10), 150 nm (BFBT-15), and 200 nm (BFBT-20), respectively. Circular platinum top electrodes of diameter 0.5 mm were sputtered on film surface to investigate electrical behavior of thin films. Crystalline structure of thin films was analyzed by using X-ray diffractometer (Phillips X-pert pro) with CuK_α (λ = 0.154 nm) radiation. The atomic force microscopic (AFM) images were explored using Nanoscope-V. The dielectric measurements were carried out using LCR meter (Wayne Kerr 6500B), and ferroelectric measurements were performed using a PE loop tracer. Magnetic measurements were carried out by VSM (Lakeshore 7304). Magnetoelectric measurements were performed on an in-house ME setup.

■ RESULTS AND DISCUSSION

Glancing angle X-ray diffraction (GAXRD) patterns, recorded at incident angle 1°, on different BFO/BTO bilayer thin films samples sputtered on $Pt/TiO_2/SiO_2/Si(100)$ substrates are shown in Figure 1. Both BFO and BTO layers were found to be
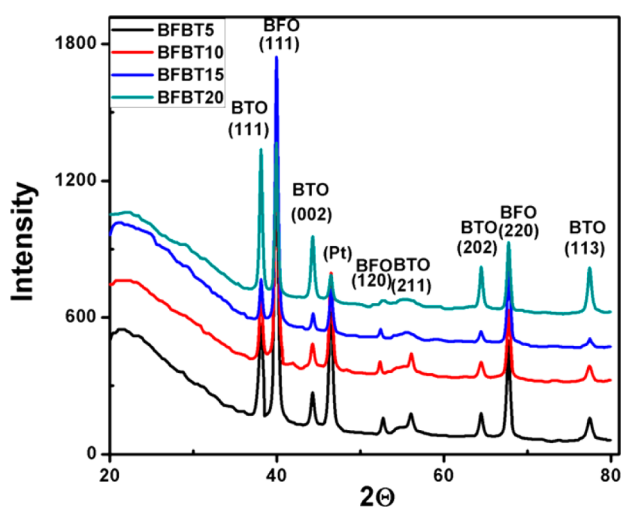
Figure 1. GAXRD patterns of bilayer thin films with increasing thickness of BFO.

polycrystalline in nature, and no impurity phases were detected. Indeed it is difficult to obtain a pure single phase BFO thin film when deposited directly on $Pt/TiO_2/SiO_2/Si(100)$ substrate even with similar buffer layers.[19,20] The orientation of films was further analyzed by X-ray diffraction performed in $\theta-2\theta$ mode. The (110) plane of BFO appeared in $\theta-2\theta$ mode only which was not be observed in GAXRD mode (Figure S1 in the Supporting Information). It confirmed that the (110) plane of BFO has a high degree of in-plane texture orientation. It can be inferred that the bottom BTO layer promotes the formation of pure perovskite phase and high degree of (110) orientation in film texture. A quantitative analysis of surface morphologies of bilayer thin films was performed using atomic force microscopy in tapping mode. A dense, crack-free surface morphology without pinholes can be observed from AFM images for all bilayer films as shown in Figure 2. Homogeneous distribution of grains and grain boundaries irrespective of increasing thickness of BFO layer has been depicted from AFM micrographs. Average grain size was calculated to be 12, 20, 24, and 30 nm for BFBT-5, 10, 15, and 20, respectively. The root-mean-square (rms) surface roughness was measured as 7.29, 4.97, 4.23, and 3.58 nm for BFBT-5, 10, 15, and 20, respectively. The morphology and nature of bilayer interface were further analyzed by cross-sectional FESEM images as
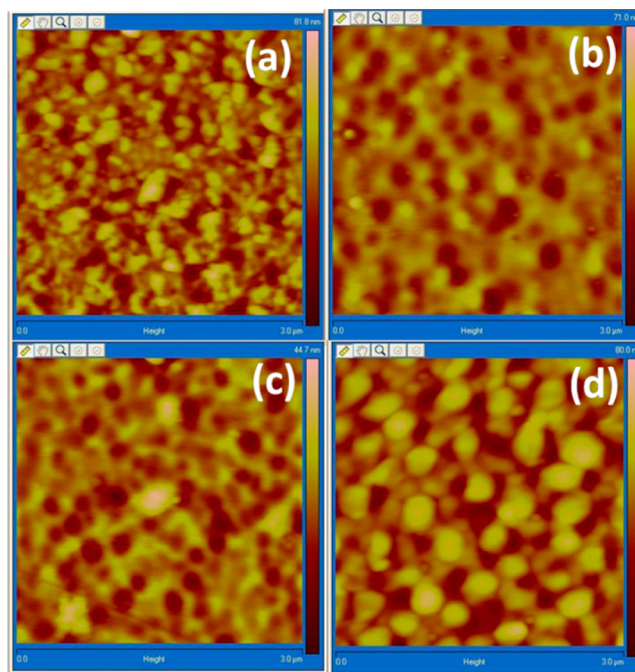

Figure 2. AFM images captured on 3 μm × 3 μm area of the different bilayer thin films: (a) BFBT-5, (b) BFBT-10, (C) BFBT-15, and (d) BFBT-20.

shown in Figure 3. Along with well-observed grains and grain boundaries of both BTO and BFO layer, an interdiffused layer of both phases was also observed at bilayer interface. A qualitative elemental analysis of bilayer film was performed by EDS spectra (Figure S2 in the Supporting Information).

Room temperature ferroelectric hysteresis loops of BFO/BTO bilayer thin films measured at frequency 50 Hz are shown in Figure 4a. All films exhibit well-saturated hysteresis loop with a large remnant polarization. A maximum value of remnant polarization ($2P_r$) ∼ 30 $\mu C/cm^2$ with coercive field ($2E_c$) ∼ 155 kV/cm was observed for BFBT-20. This value is significantly larger than previously reported value of $2P_r$ ∼ 13.7 $\mu C/cm^2$ for BFO thin film grown on BTO buffer layer.[20] The remnant polarization decreased to 22 $\mu C/cm^2$ for BFBT-15 and 20 $\mu C/cm^2$ for BFBT-10 and 18 $\mu C/cm^2$ for BFBT-5, while coercivity was found to increase with decrease in thickness of BFO layer. Large remnant polarization value of BFBT-20 as compared to other thin films can be attributed to denser microstructure and larger ferroelectric phase of the film. A decrease in grain size was clearly observed from the AFM images on reducing BFO thickness resulting into more grain boundaries. A coupling between grain boundaries and domain wall motion can severely constrain the reversible domain wall motion and increase the coercivity on reducing thickness of BFO layer.[30,31]

Magnetization measurements confirmed existence of room temperature ferromagnetism in all the films as shown in Figure 4b. $M-H$ loops are plotted after subtracting the buffered substrate signal contribution from the total signal. BFO is a G-type antiferromagnetic with Fe^{3+} magnetic moments coupled ferromagnetically within (111) planes and antiferromagnetically between adjacent planes.[32] The observed induced ferromagnetism in the bilayer thin films can be interpreted as a manifestation of the creation of unbalanced spins at the interface.[33,34] Maximum induced magnetization of the value M_s ∼ 33 emu/cc was observed in BFBT-5, which got reduced with
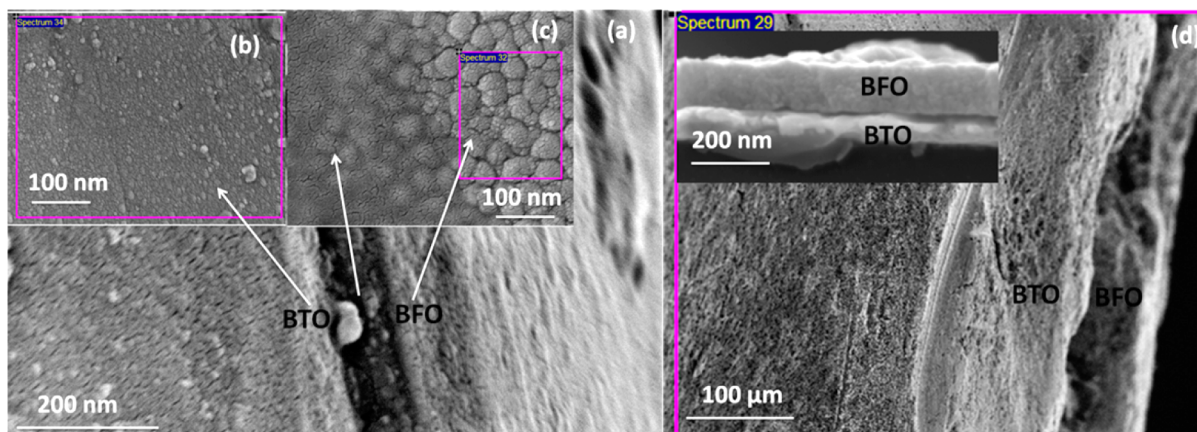
Figure 3. Cross-sectional FESEM image of bilayer thin film of BFO/BTO: (a) top view of film interface; inset (b) BTO layer; inset (C) interdiffusion and BFO layer; (d) side view bilayer interface.
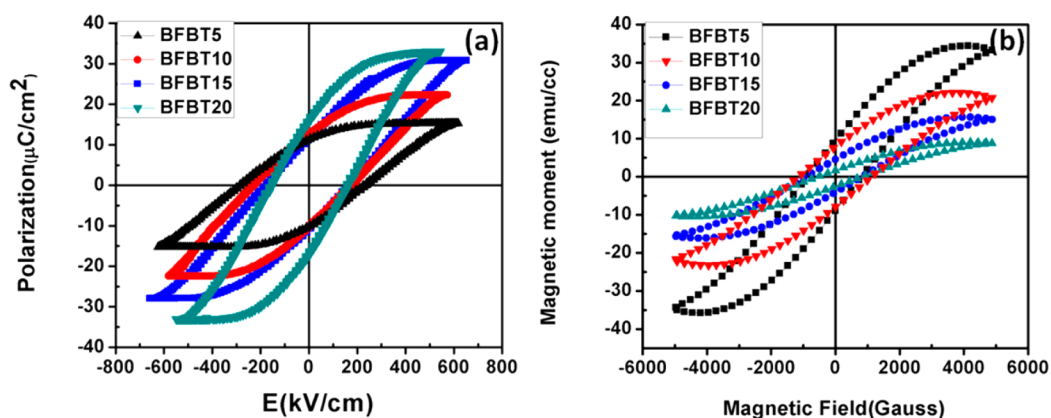
Figure 4. (a) Room temperature PE loops of BFO/BTO bilayer thin films having different BFO thicknesses. (b) Room temperature magnetization $(M-H)$ loops of bilayer thin films.

increase in the thickness of BFO layer. Saturation magnetization (M_s) values obtained were 20 emu/cc for BFBT-10 and further reduced to 15 emu/cc for BFBT-15 and 8 emu/cc for BFBT-20 thin films. For antiferromagnetic grains, decreasing particle size results in induced ferromagnetism due to incomplete surface compensation of long-range antiferromagnetic ordering at the surface of particle.[35] Decrease in particle size results in increasing surface to volume ratio and more contribution from uncompensated spins at particles surface. It results in increased magnetic moment with decreasing particle size in bilayer thin films.

The current−voltage $(J-E)$ characteristics of bilayer thin films were measured in order to explore conduction mechanism across the interface as shown in Figure 5. For positive bias (V_+) a positive voltage was applied at BFO layer and negative at BTO layer. The current was recorded after delay time of 10 s to get rid of undesirable transient response which creeps in with the change in bias voltage. Measurements were repeated by reversing the polarity of the applied voltage, i.e., for negative bias (V_-) as well. The current density $J \sim 10^{-3}$ A/cm^2 has been reported for single layer BFO thin films on similar substrate at applied electric field.[36] The observed current density in bilayer films has been found to be significantly reduced $(J \sim 10^{-6}$ A/cm^2) compared to single layer BFO thin films. Two types of conduction mechanisms have been widely studied to investigate the leakage current in ferroelectric thin films: bulk limited and interface limited current conduction. Space−charge-limited
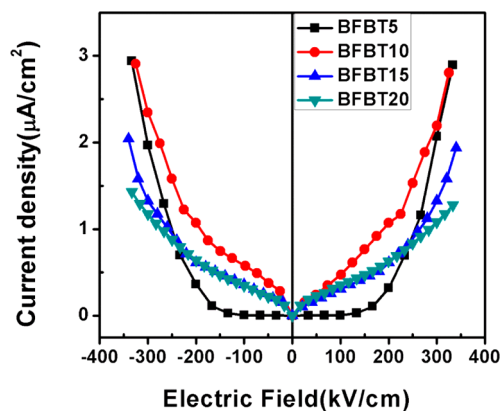

Figure 5. Current density vs electric field curves of bilayer BFO/BTO at different BFO thicknesses.

current (SCLC) and Poole−Frenkel (PF) emission are bulk limited conduction mechanisms while Schottky emission and Fowler−Nordheim (FN) tunneling constitute interface limited conduction phenomenon.[37−39] Leakage current mechanism was analyzed by fitting the observed data in reference to above stated models (Figure S3 in the Supporting Information). An ohmic-like current conduction was observed at low applied electric fields $(E \sim 150$ kV/cm) for BFBT-5, 10, and 15 bilayer films. On the other hand, at higher electric fields, an interface

Table 1. Electrical, Magnetic, and Magnetoelectric Coupling Parameters of BFO/BTO Bilayer Thin Films

	positive biasing			negative biasing			remnant polarization	magnetization	magnetoelectric coupling coefficient
composition	φ_b (meV)	α	β	φ_b (meV)	α	β	$2P_r$ (μC/cm^2)	M_s (emu/cc)	α_{ME} (mV/cm.Oe)
BFBT5	21	8.653	605	20	8.697	574	18	33	61
BFBT10	9.6	9.635	262	7.9	9.799	213	20	20	58
BFBT15	7.8	10.50	203	6.1	10.33	160	22	15	45
BFBT20	–						30	8	26
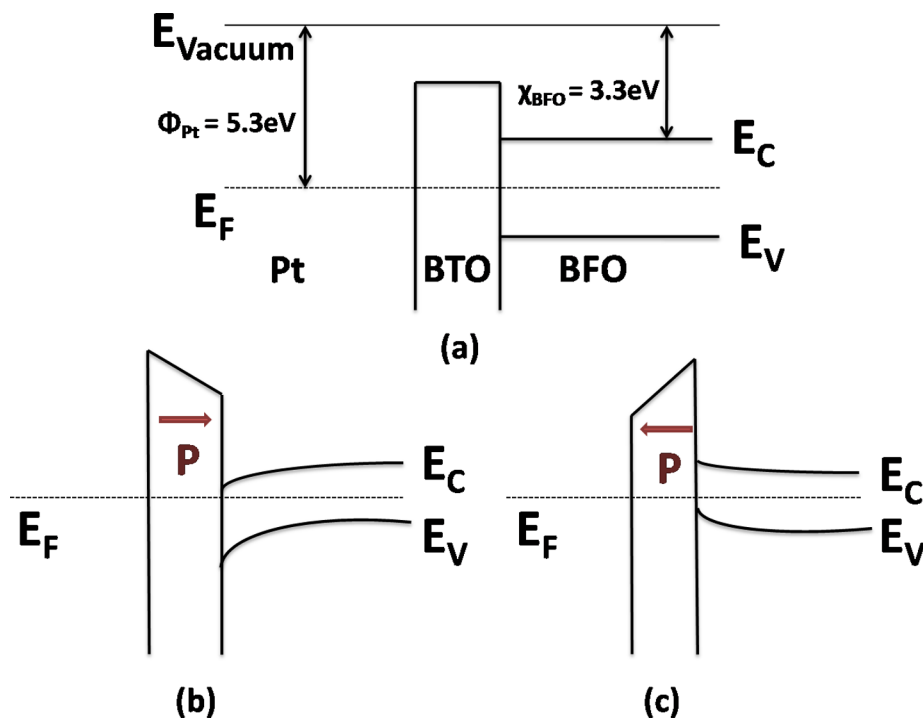
Figure 6. Band bending at bilayer interface: (a) zero biasing condition; (b) increase in potential barrier at positive biasing; (c) lowering of potential barrier at negative biasing.

limited FN tunneling dominated the current transport behavior. The interface limited FN tunneling is given by the equation

$$J = \alpha E_{ox^2} \exp\left(-\frac{\beta}{E_{ox}}\right)$$

where $\alpha = (1.54 \times 10^{-6})/(m^*\varphi_b)$, $\beta = 6.83 \times 10^{-7}(m^*)^{0.5}(\varphi_b)^{0.5}$, E_{ox} is the applied electric field, m^* is effective mass of electron, and φ_b is potential barrier involved in the tunneling conduction. The potential barrier calculated by the above equation along with the parameters is given in Table 1. The energy barrier was found to be reduced with increase in the thickness of BFO layer, and ohmic-like conduction mechanism was observed for BFBT-20 in the whole range of applied electric field. The relationship between electronic band bending and applied electric filed is

$$E = \frac{1}{q}\frac{d\phi}{dx}$$

where ϕ is intrinsic Fermi level, q is electric charge, and x is thickness of film.[40] For the same applied voltage, reducing thickness of film results in gradually increased electric field within the film. It results in stronger built-in electric field at film electrode interface which led to increase in potential barrier and immobile charges at film electrode interface at lower thickness. Larger barrier height was also observed for positive biasing as

compared to negative biasing of applied electric field. The band bending at bilayer interface is shown in Figure 6. To ascertain the role of bilayer interface on current conduction across the interface, voltage dependence of dynamic resistance and capacitance was also measured. The oscillator level for capacitance measurement was kept at 10 mV, and measuring frequency was kept at 10 kHz. Capacitance–voltage, $C(V)$, plots recorded with and without the presence of an applied magnetic field are shown in Figure 7, while the inset represents resistance–voltage, $R(V)$ profiles of the films. In ferroelectric thin film $C(V)$ profile is a typical butterfly-like curve where capacitance peaks at coercive field, but a significant asymmetry in $C(V)$ profile to a typical butterfly curve was observed in the bilayer films. It represents contribution from the interfacial charge to the electric polarization switching.[41] The total capacitance of bilayer thin film is given by

$$C_{eff} = \left(\frac{1}{C_{BTO}} + \frac{1}{C_{BFO}} + \frac{1}{C_S}\right)^{-1}$$

where C_{BTO} is the capacitance of BTO layer, C_{BFO} is the capacitance of BFO layer, and C_S is capacitance of the space charge layer at the bilayer interface. The ferroelectric polarization of BFO is weak as compared to BTO, and at the bilayer interface interdiffusion of both phases has been confirmed by FESEM images. Interdiffused interfacial layer is
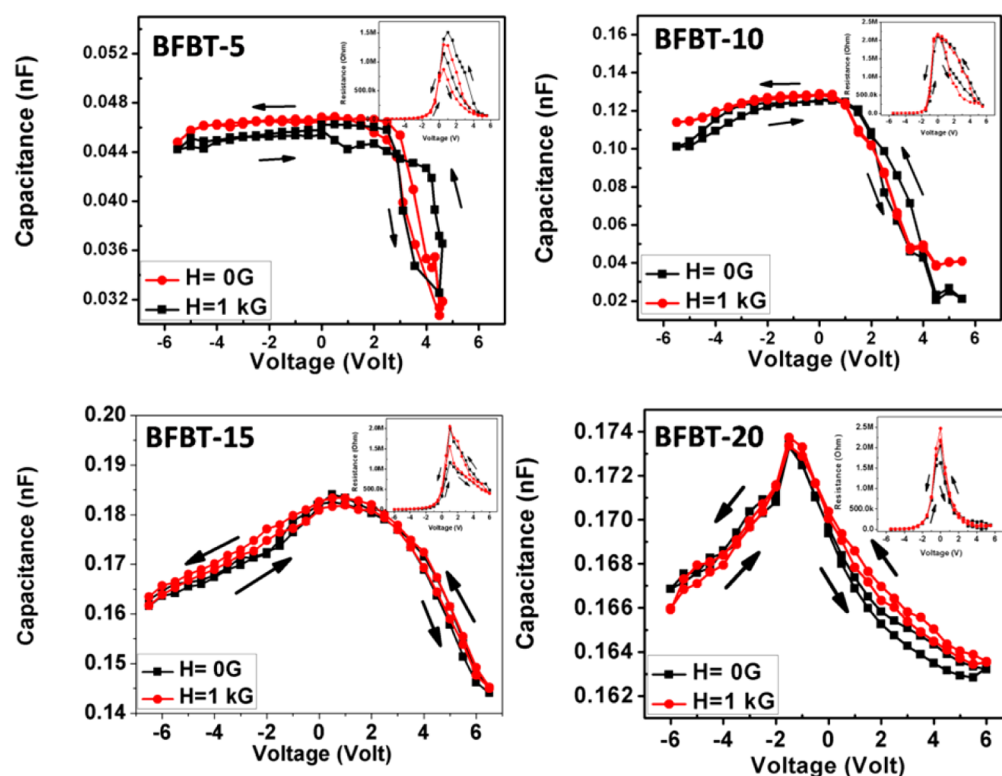
Figure 7. Capacitance−voltage curves of bilayer thin films of BFO/BTO for different thickness, inset representing hysteretic resistance switching at positive biasing.

not ferroelectrically polarizable and results in a voltage drop across the interface due to its additional capacitance. On the other hand, n-type semiconducting ferroelectric behavior of BFO is considered due to the availability of free electrons because of valence fluctuations of $Fe^{3+} \rightarrow Fe^{2+} + e^-$, which act as donor ions as confirmed by XPS results (Figure S4 in the Supporting Information). Due to the difference in polarizability of BFO and BTO, and also the availability of free charges on grain boundaries at the interface, the electric polarization is expected to be discontinuous at the interface. Positive biasing directs the ferroelectric polarization of BTO away from BFO surface resulting into negative bound charges on the BTO surface close to BFO. The negative bound charges repel electrons away from BFO surface by formation of depletion layer at bilayer interface. At large positive biasing, the effective capacitance is reduced by the increase of the associated series depletion capacitance (C_S) at the interface. It results in suppression of ferroelectric polarization which can be seen in the form of reduced C_{eff} at large positive biasing and asymmetry in $C(V)$ curves as shown in Figure 7. During increased positive biasing, immobile charge carriers present in the depletion region also result in high resistance state. During the decreasing branch of positive biasing, the reduction in the numbers of available charge carriers in the depletion region decreases the resistance and results in overall hysteretic resistance switching at positive biasing. A large change in the device resistance (∼1 M ohm) during switching from 0 to 5 V and hysteretic resistance-switching observed for applied positive biasing in $R(V)$ plots may be very useful in memristor device applications. Larger barrier height observed for positive biasing as calculated from $J−E$ results can be attributed to depletion of charge carriers at bilayer interface which enhances the barrier height for tunneling electrons across the interface as shown in Figure

6. Negative biasing directs the ferroelectric polarization of BTO toward BFO resulting in the positive bound charges at BTO surface close to BFO. Presence of positive bound charges at the bilayer interface at negative biasing results in the accumulation of electrons which can be seen in the form of almost flat slope of $C−V$ profile (C_{eff}) in the negative biasing. A shift in $C(V)$ and $R(V)$ profile with applied magnetic field indicates the coupling of interfacial charge at grain boundaries of bilayer interface with the magnetic field. A decrease in grain size resulting in more grain boundaries was observed from AFM images with decreasing thickness of BFO layer. A significant change in $C(V)$ and $R(V)$ profile with applied magnetic field in thinner films may be attributed to larger contribution from grain boundary charge and its interaction with applied magnetic field. This was further confirmed by room temperature magnetodielectric measurements.

Frequency dependence of room temperature dielectric constant (ε')/dielectric loss (tan δ) of bilayer samples is shown in Figure 8. The dielectric constant was found to be increased while dielectric loss decreased with increasing thickness of BFO layer which is in agreement with ferroelectric results. Two different peaks of dielectric relaxation can be clearly observed in Figure 8 in all thin films. Dielectric relaxation peak at lower frequency can arise either from additional capacitance of film−electrode interface or grain boundaries at bilayer interface. The intrinsic effects contribute to dielectric relaxation at high frequencies (>1 MHz), and extrinsic contribution from grain boundary capacitance or Maxwell−Wagner polarization to dielectric relaxation arises in the intermediate frequency range (∼10 kHz) while the contributions from electrode arise at lower frequency range (<1 kHz).[42] Thus, we may infer that the presence of dielectric relaxation peak near 10 kHz for all the films arises from the
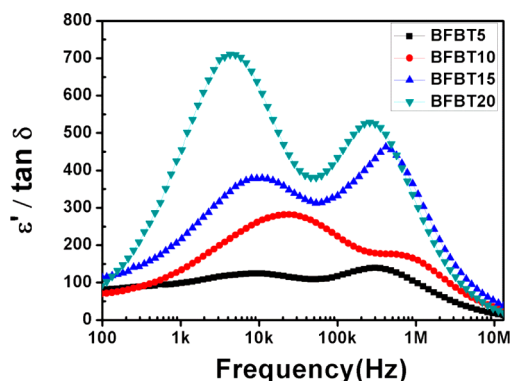
Figure 8. (a) Frequency dependence of constant (ε')/dielectric loss (tan δ) of bilayer thin films at different thickness.

additional capacitance due to some extrinsic source such as grain boundary charge at bilayer interface. High frequency relaxation peak ($\sim$1 MHz) arises from grain capacitance while contribution from the electrode is ruled out. The effect of magnetic field on dielectric relaxation peak was investigated by magnetodielectric response at room temperature. Figure 9 represents $\Delta\varepsilon'/\Delta\tan\delta$ plots as a function of frequency at different applied magnetic fields. A sharp change in $\Delta\varepsilon'/\Delta\tan\delta$ curve near 10 kHz was observed in all films. The apparent decrease in $\Delta\varepsilon'/\Delta\tan\delta$ value was due to increase in tan δ value with applied magnetic field at $\sim$10 kHz. High magnetic field dependence observed at $\sim$10 kHz compared to lower or higher frequencies indicates that magnetic field mainly affects the grain boundary charge relaxation, not the charge at grains which arise at higher frequency. This effect is more pronounced in thinner films where larger numbers of grain boundaries are present as observed from AFM images. It confirms the coupling of grain

boundary charges present at the bilayer interface with applied magnetic field which was also observed from the $C(V)$ and $R(V)$ results. It can be concluded that magnetoelectric interaction in bilayer thin films is mediated by induced charge at grain boundaries present at the bilayer interface. Interaction of interfacial charges with applied magnetic field consequently results in change in dynamic capacitance as magnetocapacitance effect in films.
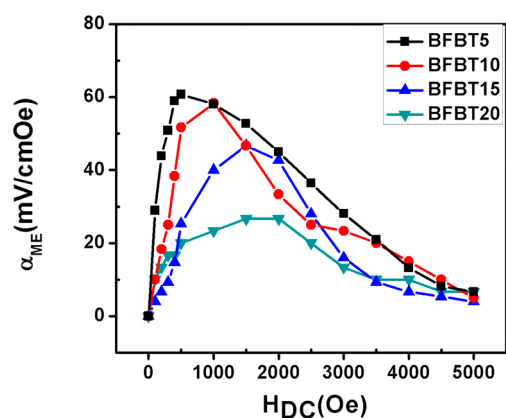
Magnetoelectric coupling coefficient (α_{ME}) was measured in bilayer films by dynamic method. Thin films were biased with ac magnetic field (δH) of 10 Oe at 999 Hz, and a dc magnetic field (H_o) was applied collinear to it. Longitudinal magnetoelectric coupling coefficient (α_{ME}) was measured by applying effective magnetic field ($H_o + \delta H$) perpendicular to the sample. The output voltage was measured by lock-in amplifier with a fixed phase relationship to the reference signal. Prior to the measurements, films were poled with electric field 100 kV/cm at 150 °C for 1 h. Magnetoelectric coupling coefficient (α_{ME}) was calculated using equation

$$\alpha_{ME} = \frac{\delta V}{\delta H \cdot t}$$

where δV is the output voltage, δH is applied ac magnetic field, and t is the thickness of the sample. The maximum calculated magnetoelectric coupling coefficient was 61 mV/cm·Oe for BFBT-5 as shown in Figure 10. Only a small variation in α_{ME} value was observed for BFBT-10 which was 58 mV/cm·Oe. With the further increase in the thickness of BFO layer, the magnetoelectric coupling coefficient reduced to 48 mV/cm·Oe for BFBT-15 and to 20 mV/cm·Oe for BFBT-20 thin films.
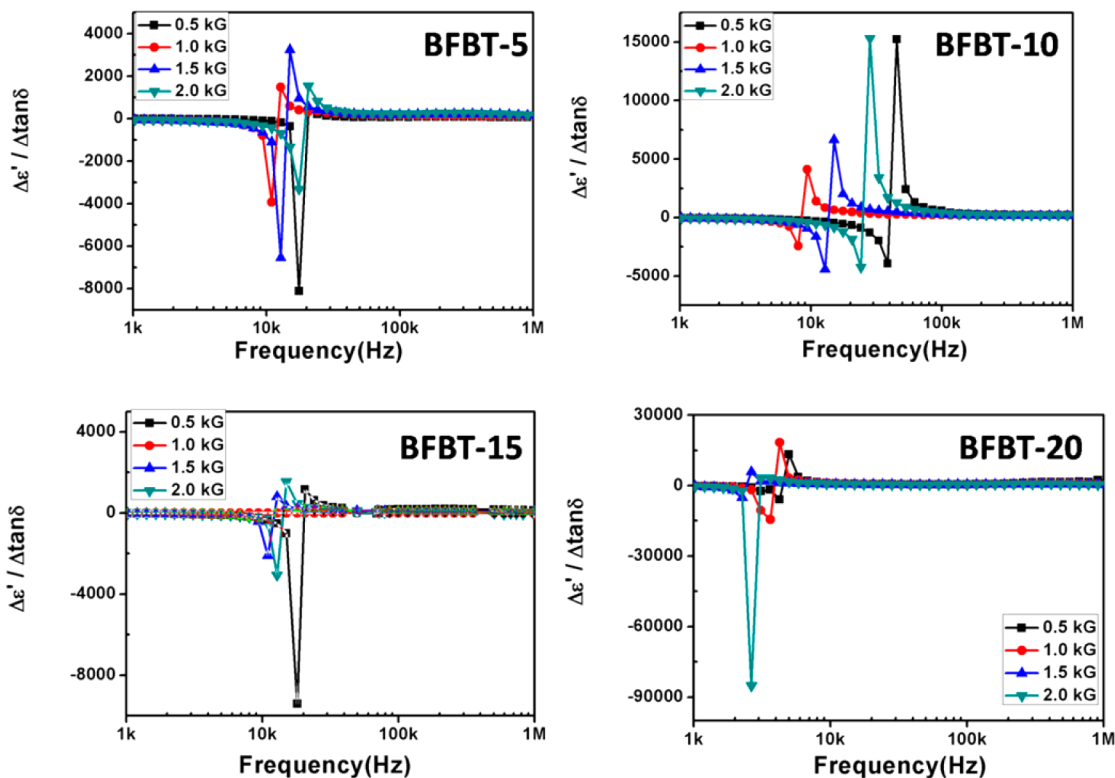
Figure 9. Frequency dependence of $\Delta\varepsilon'/\Delta$ tan δ at different applied magnetic fields.

Figure 10. Magnetoelectric coupling coefficient in longitudinal direction for BFO/BTO bilayer at different thickness.

CONCLUSIONS

Bilayer thin films of pure phase BFO/BTO have been prepared. Significantly improved room temperature multiferroic properties were observed as compared to the polycrystalline pure BFO thin films in identical conditions. Depletion and accumulation of charges at the bilayer interface have been analyzed by hysteretic resistance switching and capacitance−voltage profiles. It was further investigated by current−voltage characteristics of bilayer films wherein interface limited current conduction has been affected by ferroelectric polarization. The shifting of dynamic resistance and capacitance with applied magnetic field was further analyzed by magnetodielectric as well as magnetoelectric-coupling coefficient measurement. A room temperature magnetocapacitance was found to originate from induced charge at the bilayer interface which can be manipulated by varying thickness of BFO to obtain higher ME coupling coefficient. Dynamic magnetoelectric coupling was investigated, and maximum longitudinal magnetoelectric coupling was observed to be 61 mV/cm·Oe in bilayer having 50 nm thin $BiFeO_3$. The observation of induced room temperature magnetoelectric coupling from the interfacial charge in magnetoelectric bilayer is significant for the applications related to memory and spintronic devices.

ASSOCIATED CONTENT

Ⓢ Supporting Information

XRD plots of bilayer films in $\theta-2\theta$ mode; EDS spectra of bilayer films; Fowler−Nordheim (FN) tunneling plots of thin film; XPS spectra of bilayer film; resistance−voltage switching characteristics. This material is available free of charge via the Internet at http://pubs.acs.org/.

AUTHOR INFORMATION

Corresponding Author
*Fax: 91-11-45609310. Phone: 91-11-45608599. E-mail: rkkotnala@nplindia.org, rkkotnala@gmail.com.

Notes
The authors declare no competing financial interest.

ACKNOWLEDGMENTS

REFERENCES

(1) Eerenstein, W.; Mathur, N. D.; Scott, J. F. Multiferroic and Magnetoelectric Materials. *Nature* **2006**, *442*, 759−765.

(2) Spaldin, N. A.; Fiebig, M. The Renaissance of Magnetoelectric Multiferroics. *Science* **2005**, *309*, 391−392.

(3) Valencia, S.; Crassous, A.; Bocher, L.; Garcia, V.; Moya, X.; Cherifi, R. O.; Deranlot, C.; Bouzehouane, K.; Fusil, S.; Zobelli, A.; Gloter, A.; Mathur, N. D.; Gaupp, A.; Abrudan, R.; Radu, F.; Barthélémy, A.; Bibes, M. Interface-Induced Room-Temperature Multiferroicity in $BaTiO_3$. *Nat. Mater.* **2011**, *10*, 753−758.

(4) Liu, M.; Obi, O.; Lou, J.; Chen, Y.; Cai, Z.; Stoute, S.; Espanol, M.; Lew, M.; Situ, X.; Ziemer, K. S.; Harris, V. G.; Sun, N. X. Giant Electric Field Tuning of Magnetic Properties in Multiferroic Ferrite/Ferroelectric Heterostructures. *Adv. Funct. Mater.* **2009**, *19*, 1826−1831.

(5) Duan, C. G.; Jaswal, S. S.; Tsymbal, E. Y. Predicted Magnetoelectric Effect in $Fe/BaTiO_3$ Multilayers: Ferroelectric Control of Magnetism. *Phys. Rev. Lett.* **2006**, *97*, 047201−4.

(6) Lage, E.; Kirchhof, C.; Hrkac, V.; Kienle, L.; Jahns, R.; Knöchel, R.; Quandt, E.; Meyners, D. Exchange Biasing in Magnetoelectric Composites. *Nat. Mater.* **2012**, *11*, 523−529.

(7) Laletin, U.; Sreenivasulu, G.; Petrov, V. M.; Garg, T.; Kulkarni, A. R.; Venkataramani, N.; Srinivasan, G. Hysteresis and Remanence in Magnetoelectric Effects in Functionally Graded Magnetostrictive-Piezoelectric Layered Composites. *Phys. Rev. B* **2012**, *85*, 104404−8.

(8) Thiele, C.; Dörr, K.; Bilani, O.; Rödel, J.; Schultz, L. Influence of Strain on the Magnetization and Magnetoelectric Effect in $La_{0.7}A_{0.3}MnO_3$/PMN-PT(001) (A = Sr, Ca). *Phys. Rev. B* **2007**, *75*, 054408−8.

(9) Kida, N.; Yamada, H.; Sato, H.; Arima, T.; Kawasaki, M.; Akoh, H.; Tokura, Y. Optical Magnetoelectric Effect of Patterned Oxide Superlattices with Ferromagnetic Interfaces. *Phys. Rev. Lett.* **2007**, *99*, 197404−4.

(10) Zheng, H.; Zhan, Q.; Zavaliche, F.; Sherburne, M.; Straub, F.; Cruz, M. P.; Chen, L. Q.; Dahmen, U.; Ramesh, R. Controlling Self-Assembled Perovskite−Spinel Nanostructures. *Nano Lett.* **2006**, *6*, 1401−1407.

(11) Shah, J.; Kotnala, R. K. Induced Magnetism and Magnetoelectric Coupling in Ferroelectric $BaTiO_3$ by Cr-Doping Synthesized by a Facile Chemical Route. *J. Mater. Chem. A* **2013**, *1*, 8601−8608.

(12) Shah, J.; Kotnala, R. K. Magnetoelectric Coupling of Multiferroic Chromium Doped Barium Titanate Thin Film Probed by Magneto Impedance Spectroscopy. *Appl. Phys. Lett.* **2014**, *104*, 142901−5.

(13) Bhattacharjee, S.; Panday, V.; Kotnala, R. K.; Pandey, D. Unambiguous Evidence for Magnetoelectric Coupling of Multiferroic Origin in 0.73 $BiFeO_3$−0.27 $PbTiO_3$. *Appl. Phys. Lett.* **2009**, *94*, 012906−3.

(14) Verma, K. C.; Kotnala, R. K.; Negi, N. S. Improved Dielectric and Ferromagnetic Properties of Fe-Doped $PbTiO_3$ Nanoparticles at Room Temperature. *Appl. Phys. Lett.* **2008**, *92*, 152902−3.

(15) Eerenstein, W.; Wiora, M.; Prieto, J. L.; Scott, J. F.; Mathur, N. D. Giant Sharp and Persistent Converse Magnetoelectric Effects in Multiferroic Epitaxial Heterostructures. *Nat. Mater.* **2007**, *6*, 348−351.

(16) Lou, J.; Liu, M.; Reed, D.; Ren, Y.; Sun, N. X. Giant Electric Field Tuning of Magnetism in Novel Multiferroic FeGaB/Lead Zinc Niobate−Lead Titanate (PZN−PT) Heterostructures. *Adv. Mater.* **2009**, *21*, 4711−4715.

(17) Hu, J. M.; Nan, C. W.; Chen, L. Q. Size-Dependent Electric Voltage Controlled Magnetic Anisotropy in Multiferroic Heterostructures: Interface-Charge and Strain Co-Mediated Magnetoelectric Coupling. *Phys. Rev. B* **2011**, *83*, 134408−6.

(18) Catalan, G.; Scott, J. F. Physics and Applications of Bismuth Ferrite. *Adv. Mater.* **2009**, *21*, 2463−2485.

(19) Wu, J. G.; Kang, G. Q.; Liu, H. J.; Wang, J. Ferromagnetic, Ferroelectric and Fatigue Behavior of (111)-Oriented $BiFeO_3$/(Bi 1/2 Na 1/2)TiO_3 Lead-Free Bilayered Thin Films. *Appl. Phys. Lett.* **2009**, *94*, 172906−3.

(20) Yang, P.; Kim, K. M.; Joh, Y. G.; Kim, D. H.; Lee, J. Y.; Zhu, J. S.; Lee, H. Y. Effect of $BaTiO_3$ Buffer Layer on Multiferroic Properties of $BiFeO_3$ Thin Films. *J. Appl. Phys.* **2009**, *105*, 061618−4.

(21) Xie, D.; Zang, Y.; Luo, Y.; Han, X.; Ren, T.; Liu, L. Structural, Ferroelectric, Dielectric, and Magnetic Properties of $BiFeO_3/Bi_{3.15}Nd_{0.85}Ti_3O_{12}$ Multilayer Films Derived by Chemical Solution Deposition. *J. Appl. Phys.* **2009**, *105*, 084109−5.

(22) Cheng, Z.; Wang, X.; Kannan, C. V.; Ozawa, K.; Kimura, H.; Nishida, T.; Zhang, S.; Shrout, T. R. Enhanced Electrical Polarization and Ferromagnetic Moment in a Multiferroic $BiFeO_3/Bi_{3.25}Sm_{0.75}Ti_{2.98}V_{0.02}O_{12}$ Double-Layered Thin Film. *Appl. Phys. Lett.* **2006**, *88*, 132909−3.

(23) Wu, J.; Wang, J. Improved Ferroelectric and Fatigue Behavior of $Bi_{0.95}Gd_{0.05}FeO_3/BiFe_{0.95}Mn_{0.05}O_3$ Bilayered Thin Films. *J. Phys. Chem. C* **2010**, *114*, 19318−19321.

(24) Huang, F.; Lu, X.; Lin, W.; Cai, W.; Wu, X.; Kan, Y.; Sang, H.; Zhu, J. Multiferroic Properties and Dielectric Relaxation of $BiFeO_3/Bi_{3.25}La_{0.75}Ti_3O_{12}$ Double-Layered Thin Films. *Appl. Phys. Lett.* **2005**, *90*, 252903−3.

(25) Singh, A.; Pandey, V.; Kotnala, R. K.; Pandey, D. Direct Evidence for Multiferroic Magnetoelectric Coupling in $0.9BiFeO_3$−$0.1BaTiO_3$. *Phys. Rev. Lett.* **2008**, *101*, 247602−4.

(26) Ueda, K.; Tabata, H.; Kawai, T. Coexistence of Ferromagnetism and Ferroelectricity in $BiFeO_3$−$BaTiO_3$ Thin Films at Room Temperature. *Appl. Phys. Lett.* **1999**, *75*, 555−557.

(27) Kumar, M. M.; Srinivas, A.; Suryanarayana, S. V. Structure Property Relations in $BiFeO_3/BaTiO_3$ Solid Solutions. *J. Appl. Phys.* **2000**, *87*, 855−862.

(28) Gupta, R.; Shah, J.; Singh, S.; Chaudhary, S.; Kotnala, R. K. Magnetoelectric Coupling Induced Anisotropy in Multiferroic Nanocomposite $(1−x)BiFeO_3−xBaTiO_3$. *J. Nanopart. Res.* **2013**, *15*, 2004−8.

(29) Wang, T. H.; Tu, C. S.; Chen, H. Y.; Ding, Y.; Lin, T. C.; Yao, Y. D.; Schmidt, V. H.; Wu, K. T. Magnetoelectric Coupling and Phase Transition in $BiFeO_3$ and $(BiFeO_3)0.95−(BaTiO_3)0.05$ Ceramics. *J. Appl. Phys.* **2011**, *109*, 044101−4.

(30) Marincel, D. M.; Zhang, H.; Kumar, A.; Jesse, S.; Kalinin, S. V.; Rainforth, W. M.; Reaney, I. M.; Randall, C. A.; Mckinstry, S. T. Influence of a Single Grain Boundary on Domain Wall Motion in Ferroelectrics. *Adv. Funct. Mater.* **2014**, *24*, 1409−1417.

(31) Xu, F.; Mckinstry, S. T.; Ren, W.; Xu, B.; Xie, Z. L.; Hemker, K. J. Domain Wall Motion and Its Contribution to Dielectric and Piezoelectric Properties of Lead Zirconate Titanate Films. *J. Appl. Phys.* **2001**, *89*, 1336−1348.

(32) Ruette, B.; Zvyagin, S.; Pyatakov, A. P.; Bush, A.; Li, J. F.; Belotelov, V. I.; Zvezdin, A. K.; Viehland, D. Magnetic-Field-Induced Phase Transition in $BiFeO_3$ Observed by High-Field Electron Spin Resonance: Cycloidal to Homogeneous Spin Order. *Phys. Rev. B* **2004**, *69*, 064114−7.

(33) Wang, J.; Neaton, J. B.; Zheng, H.; Nagarajan, N.; Ogale, S. B.; Liu, B.; Viehland, D.; Vaithyanathan, V.; Schlom, D. G.; Wagmare, U. V.; Spaldin, N. A.; Rabe, K. M.; Wuttig, M.; Ramesh, R. Epitaxial $BiFeO_3$ Multiferroic Thin Film Heterostructures. *Science* **2003**, *299*, 1719−1722.

(34) Edere, C.; Spaldin, N. A. Weak Ferromagnetism and Magnetoelectric Coupling in Bismuth Ferrite. *Phys. Rev. B* **2005**, *71*, 060401−4.

(35) Richardson, J. T.; Yiagas, D. I.; Turk, D.; Forster, K.; Twig, M. V. Origin of Superparamagnetism in Nickel Oxide. *J. Appl. Phys.* **1991**, *70*, 6977−6982.

(36) Yang, H.; Jain, M.; Suvorova, N. A.; Zhou, H.; Luo, H. M.; Feldmann, D. M.; Dowden, P. C.; De Paula, R. F.; Foltyn, S. R.; Jia, Q. X. Temperature-Dependent Leakage Mechanisms of $Pt/BiFeO_3/SrRuO_3$ Thin Film Capacitors. *Appl. Phys. Lett.* **2007**, *91*, 072911−3.

(37) Dawber, M.; Rabe, K. M.; Scott, J. F. Physics of Thin Film Ferroelectric Oxides. *Rev. Mod. Phys.* **2005**, *77*, 1083−1129.

(38) Waser, R.; Klee, M. Theory of Conduction and Breakdown in Perovskite Thin Films. *Integr. Ferroelectr.* **1992**, *2*, 23−40.

(39) Zhang, X. G.; Pantelides, S. T. Theory of Space Charge Limited Currents. *Phys. Rev. Lett.* **2012**, *108*, 266602−5.

(40) Lin, C. H.; Friddle, P. A.; Ma, C. H.; Daga, A.; Chen, H. Effects of Thickness on the Electrical Properties of Metalorganic Chemical Vapor Deposited $Pb(Zr,Ti)O_3$ (25−100 nm) Thin Films on $LaNiO_3$ Buffered Si. *J. Appl. Phys.* **2001**, *90*, 1509−1515.

(41) Chen, P. J.; Montgomery, S. T. A Macroscopic Theory for the Existence of the Hysteresis and Butterfly Loops in Ferroelectricity. *Ferroelectrics* **1980**, *23*, 199−207.

(42) Jonscher, A. K. Dielectric Relaxation in Solids. *J. Phys. D: Appl. Phys.* **1999**, *32*, 57−70.